Mitochondrial calcium overload is a key determinant in heart failure

Gaetano Santulli[a,b,1,2], Wenjun Xie[a,b,1], Steven R. Reiken[a,b], and Andrew R. Marks[a,b,c,2]

[a]Department of Physiology and Cellular Biophysics, College of Physicians & Surgeons, Columbia University Medical Center, New York, NY 10032; [b]Helen and Clyde Wu Center for Molecular Cardiology, College of Physicians & Surgeons, Columbia University Medical Center, New York, NY 10032; and [c]Department of Medicine, College of Physicians & Surgeons, Columbia University Medical Center, New York, NY 10032

Contributed by Andrew R. Marks, July 6, 2015 (sent for review June 15, 2015; reviewed by Geoffrey S. Pitt)

Calcium (Ca^{2+}) released from the sarcoplasmic reticulum (SR) is crucial for excitation–contraction (E–C) coupling. Mitochondria, the major source of energy, in the form of ATP, required for cardiac contractility, are closely interconnected with the SR, and Ca^{2+} is essential for optimal function of these organelles. However, Ca^{2+} accumulation can impair mitochondrial function, leading to reduced ATP production and increased release of reactive oxygen species (ROS). Oxidative stress contributes to heart failure (HF), but whether mitochondrial Ca^{2+} plays a mechanistic role in HF remains unresolved. Here, we show for the first time, to our knowledge, that diastolic SR Ca^{2+} leak causes mitochondrial Ca^{2+} overload and dysfunction in a murine model of postmyocardial infarction HF. There are two forms of Ca^{2+} release channels on cardiac SR: type 2 ryanodine receptors (RyR2s) and type 2 inositol 1,4,5-trisphosphate receptors (IP3R2s). Using murine models harboring RyR2 mutations that either cause or inhibit SR Ca^{2+} leak, we found that leaky RyR2 channels result in mitochondrial Ca^{2+} overload, dysmorphology, and malfunction. In contrast, cardiac-specific deletion of IP3R2 had no major effect on mitochondrial fitness in HF. Moreover, genetic enhancement of mitochondrial antioxidant activity improved mitochondrial function and reduced posttranslational modifications of RyR2 macromolecular complex. Our data demonstrate that leaky RyR2, but not IP3R2, channels cause mitochondrial Ca^{2+} overload and dysfunction in HF.

ryanodine receptor | heart failure | mitochondria | calcium | IP3 receptor

Type 2 ryanodine receptor/Ca^{2+} release channel (RyR2) and type 2 inositol 1,4,5-trisphosphate receptor (IP3R2) are the major intracellular Ca^{2+} release channels in the heart (1–3). RyR2 is essential for cardiac excitation–contraction (E–C) coupling (2), whereas the role of IP3R2 in cardiomyocytes is less well understood (3). E–C coupling requires energy in the form of ATP produced primarily by oxidative phosphorylation in mitochondria (4–8).

Both increased and reduced mitochondrial Ca^{2+} levels have been implicated in mitochondrial dysfunction and increased reactive oxygen species (ROS) production in heart failure (HF) (6, 7, 9–17). Albeit Ca^{2+} is required for activation of key enzymes (i.e., pyruvate dehydrogenase phosphatase, isocitrate dehydrogenase, and α-ketoglutarate dehydrogenase) in the tricarboxylic acid (also known as Krebs) cycle (18, 19), excessive mitochondrial Ca^{2+} uptake has been associated with cellular dysfunction (14, 20). Furthermore, the exact source of mitochondrial Ca^{2+} has not been clearly established. Given the intimate anatomical and functional association between the sarcoplasmic reticulum (SR) and mitochondria (6, 21, 22), we hypothesized that SR Ca^{2+} release via RyR2 and/or IP3R2 channels in cardiomyocytes could lead to mitochondrial Ca^{2+} accumulation and dysfunction contributing to oxidative overload and energy depletion.

Results and Discussion

Increased Mitochondrial Ca^{2+} in Failing Hearts. Cardiac mitochondrial Ca^{2+} (Fig. 1 *A–D* and Fig. S1) and ROS (Fig. 1*E*) were significantly elevated in mice following myocardial infarction (MI).

To determine whether the observed mitochondrial Ca^{2+} overload in failing hearts can be caused by SR Ca^{2+} leak via RyR2, we used a murine model harboring a mutation that renders the channels leaky (RyR2-S2808D) and a second model (RyR2-S2808A) with RyR2 channels protected against leak. Ca^{2+} sparks frequency (diastolic openings of RyR2 channels that reflect SR Ca^{2+} leak) was significantly increased (Fig. S2*A*), and SR Ca^{2+} load reduced (Fig. S2*B*) in cardiomyocytes from RyR2-S2808D mice compared with WT and RyR2-S2808A cardiomyocytes.

Notably, RyR2-mediated SR Ca^{2+} leak (Fig. S2) was associated with increased mitochondrial Ca^{2+} (Fig. 1 *A* and *D*) and ROS production (Fig. 1*E*). Constitutive cardiac SR Ca^{2+} leak via RyR2 (RyR2-S2808D mice) resulted in dysmorphic and malfunctioning mitochondria (Fig. S3). We observed a marked reduction in mitochondrial size (Fig. S3*D*), aspect ratio (Fig. S3*G*), and form factor (Fig. S3*H*) in left ventricular cardiomyocytes harboring leaky RyR2 channels, reflecting a low fusion-to-fission ratio. These data indicate that intracellular Ca^{2+} leak via RyR2 correlates with augmented mitochondrial fragmentation, strongly supporting a functional role for Ca^{2+} in regulating mitochondrial morphological dynamism.

Importantly, our data showing increased cardiac mitochondrial Ca^{2+} in HF, determined in absolute values in isolated organelles (Fig. 1*A*) and confirmed in dynamic evaluations at the cellular level (Fig. 1 *B–D* and Fig. S1), reconcile conflicting reports concerning mitochondrial Ca^{2+} in failing hearts (7, 10, 12, 13, 15, 17).

Significance

We demonstrate that intracellular Ca^{2+} leak causes mitochondrial Ca^{2+} overload and dysfunction in postischemic heart failure (HF). In particular, sarcoplasmic reticulum (SR) Ca^{2+} leak via type 2 ryanodine receptor (RyR2)—but not type 2 inositol 1,4,5-trisphosphate receptor (IP3R2)—channels plays a fundamental role in the pathophysiology of mitochondrial Ca^{2+} overload and dysfunction in HF. We present here a previously undisclosed molecular mechanism in HF with crucial implications in cardiac physiology. Indeed, our data establish a feedback loop between SR and mitochondria in which SR Ca^{2+} leak triggers mitochondrial dysfunction and increases the production of free radicals, which in turn lead to posttranslational modifications of RyR2 and enhance intracellular Ca^{2+} leak, thereby contributing to impaired cardiac function after myocardial infarction.

Author contributions: G.S. and A.R.M. designed research; G.S. and W.X. performed research; S.R.R. contributed new reagents/analytic tools; G.S. and A.R.M. analyzed data; and G.S. and A.R.M. wrote the paper.

Reviewers included: G.S.P., Duke University.

Conflict of interest statement: A.R.M. is a consultant and member of the board of ARMGO, which is targeting RyR channels for therapeutic purposes.

[1]G.S. and W.X. contributed equally to this work.

[2]To whom correspondence may be addressed. Email: gsantulli001@gmail.com or arm42@cumc.columbia.edu.

This article contains supporting information online at www.pnas.org/lookup/suppl/doi:10.1073/pnas.1513047112/-/DCSupplemental.

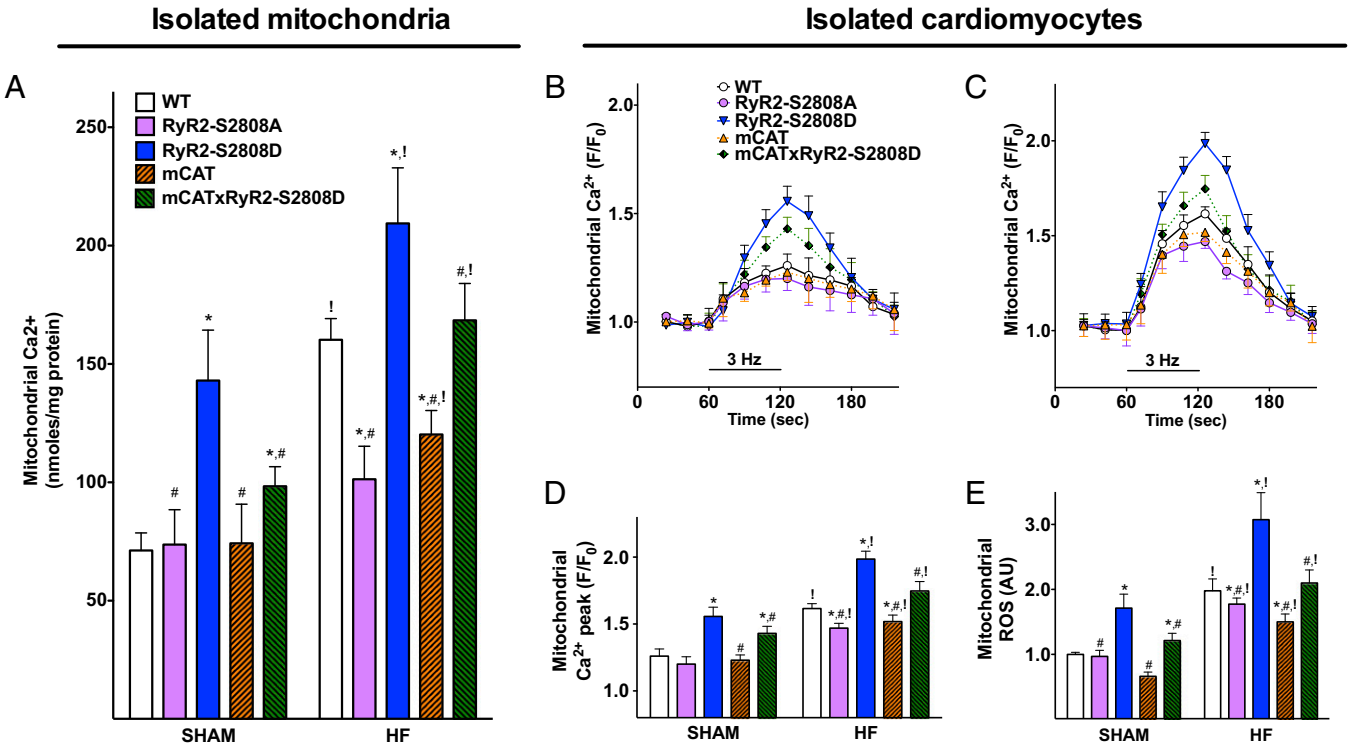

Fig. 1. Increased mitochondrial Ca^{2+} in post-MI heart failure. (*A*) Direct measurement of total Ca^{2+} content in mitochondria isolated from sham or failing ventricular samples of 6-mo-old WT, RyR2-S2808A, RyR2-S2808D, mCAT, and mCAT × RyR2-S2808D mice. Mitochondria were purified from ≥6 mice in each experimental group. (*B–D*) Mitochondrial Ca^{2+} dynamics in response to 3 Hz in cardiomyocytes (n = 22–35) enzymatically isolated from at least 7 mice per group isolated from the indicated groups. (*E*) Mitochondrial ROS generation in ventricular cardiomyocytes isolated from the indicated mice using the mitochondria-targeted fluorescent indicator of superoxide production MitoSOX Red; n > 120 ventricular myocytes from ≥4 mice in each group. Data shown represent mean ± SEM from triplicate experiments. $^{*}P < 0.05$ vs. WT; $^{\#}P < 0.05$ vs. RyR2-S2808D, ANOVA, Tukey–Kramer post hoc test; $^{!}P < 0.05$ vs. SHAM, two-tailed t test. AU, arbitrary units; ROS, reactive oxygen species.

Effects of Redox Imbalance on RyR2 Channel in Postischemic HF. We have previously shown that protein kinase A (PKA) phosphorylation and oxidation of RyR2 channels cause SR Ca^{2+} leak and contribute to HF progression (1, 2). HF-related PKA phosphorylation—in part also attributable to decreased cAMP type 4 phosphodiesterase, PDE4D3, in the RyR2 channel complex (23)—nitrosylation, and oxidation of RyR2 were attenuated in a mouse model (mCAT) with decreased ROS levels obtained via targeted overexpression of human catalase in mitochondria (Fig. 2 *A–D*).

Reduced binding of the RyR2 stabilizing subunit calstabin2 (24) to the channel due to RyR2 oxidation and PKA phosphorylation causes spontaneous diastolic SR Ca^{2+} release contributing to cardiac dysfunction in HF (1, 2). Genetically reducing RyR2 oxidation (mCAT mice) or preventing RyR2 PKA phosphorylation (RyR2-S2808A mice harboring RyR2 channels that cannot be PKA-phosphorylated) improved calstabin2 and PDE4D3 binding to RyR2 (Fig. 2 *A–F*) and cardiac performance (Fig. 2*G* and Table S1) after MI. Mitochondrial morphology (Fig. 3 *A–I* and Fig. S4) and function (Fig. 3 *J–M* and Table S2) were also improved in mCAT mice.

Oxidative overload in cardiomyocytes originates from multiple sources, including mitochondria, NAD(P)H oxidase, xanthine oxidase, and uncoupled nitric oxide synthase (16, 25, 26). Mitochondrial-derived ROS are elevated during cardiac overload or ischemic stress (4, 26, 27). Mitochondrial membrane potential, $\Delta\psi_m$, is closely linked to Ca^{2+} levels and to mitochondrial ROS production; indeed, depolarized mitochondria produce more ROS, leading to further organelle depolarization, resulting in a vicious cycle. The decrease in $\Delta\psi_m$ observed in mitochondria from RyR2-S2808D ventricular cardiomyocytes (Fig. S3*J*) is consistent with a progressive decline in $\Delta\psi_m$ due to increasing $[Ca^{2+}]$ in cardiac mitochondria and is most likely due to elevated cytosolic $[Ca^{2+}]$ caused by RyR2-mediated SR Ca^{2+} leak (10). Supporting this view, mitochondria exposed to elevated $[Ca^{2+}]$ exhibit reduced $\Delta\psi_m$, due to the large mitochondrial Ca^{2+} current generated during local $[Ca^{2+}]$ transients (28).

Ventricular cardiomyocytes harboring constitutively leaky RyR2 channels exhibited a reduction in mitochondrial ATP content and generation (Fig. S3 *L* and *M*), consistent with previous observations in failing human hearts (6). Further studies are needed to investigate in detail other systems, including neurohormonal and (epi)genetic mechanisms, endoplasmic reticulum (ER) stress, necrosis/apoptosis, and autophagy, that might participate in the regulation of bioenergetic homeostasis in HF (5, 6, 19, 25, 29).

Distinctive Roles of RyR2 and IP3R2 in the Pathophysiology of Mitochondrial Dysfunction in HF. To determine the source of SR Ca^{2+} leak that causes mitochondrial overload in failing hearts, we investigated the roles of the two major Ca^{2+} release channels on myocardial SR: RyR2 and IP3R2 (1).

We generated a murine model ($IP3R2^{CVKO}$) in which IP3R2 expression was specifically ablated in ventricular cardiomyocytes via *Cre/Lox* recombination (Fig. S5 *A–E*). $IP3R2^{CVKO}$ mice survived to adulthood without alterations in baseline myocardial function, and there was no up-regulation of the other two isoforms of IP3R (IP3R1 and IP3R3) (Fig. S5 *F* and *G*). Ca^{2+} sparks, SR Ca^{2+} load (Fig. S6), mitochondrial Ca^{2+} level (Fig. S6*C* and Fig. S7 *A* and *B*), and ROS production (Fig. S6*D*) were not significantly changed in $IP3R2^{CVKO}$ ventricular cardiomyocytes evaluated both in sham or post-MI mice. Myocardial mitochondria from $IP3R2^{CVKO}$ mice were normal (Fig. 4), and there was no

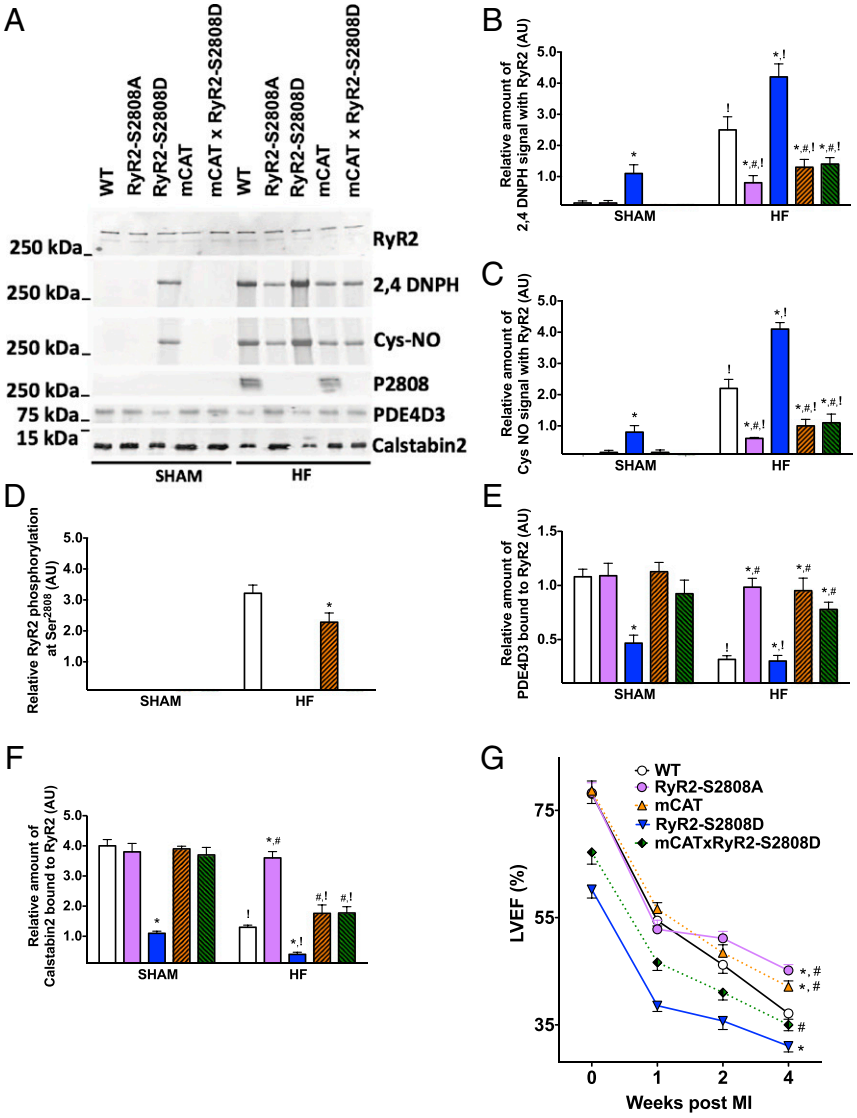

Fig. 2. Posttranslational modifications of RyR2 complex and HF progression post-MI. (*A*) Biochemical evaluation of RyR2 macromolecular complex in left ventricular samples from sham and heart failure (HF) mice. To determine channel oxidation, the carbonyl groups in the protein side chains of immunoprecipitated RyR2 were derivatized to 2,4 dinitrophenylhydrazone (2,4 DNPH) by reaction with 2,4 dinitrophenylhydrazine. The 2,4 DNPH signal associated with RyR2 was determined by anti-DNP antibody (specificity for RyR2 was achieved due to immunoprecipitation of the protein). Anti-Cys NO antibody analysis of immunoprecipitated RyR2 was used to measure RyR2 nitrosylation. Quantification of RyR2 oxidation (*B*), Cys-nitrosylation (*C*), phosphorylation at Ser^{2808} (*D*), PDE4D3 (*E*), and calstabin2 (*F*) bound to RyR2; note that constitutive phosphorylation of Ser^{2808}, mimicked by the aspartate residue substitution in RyR2-S2808D mice, cannot be detected. Data shown represent mean ± SEM from triplicate experiments. $^{*}P < 0.05$ vs. WT; $^{\#}P < 0.05$ vs. RyR2-S2808D, ANOVA, Tukey–Kramer post hoc test; $^{!}P < 0.05$ vs. SHAM, two-tailed *t* test. (*G*) Progressive cardiac dysfunction after myocardial infarction (MI) assessed by serial echocardiographic analyses. LVEF, left ventricular ejection fraction. Data are shown as mean ± SEM; $^{*}P < 0.05$ vs. WT; $^{\#}P < 0.05$ vs. RyR2-S2808D; ANOVA repeated measures; $n = 16–20$ per group. AU, arbitrary units. See also Table S1.

major effect on acute HF progression (Fig. S7*C* and Table S1). Further investigations are warranted to explore the potential role of IP3R2 in ischemia/reperfusion and in long-term ischemic HF, especially given the reported involvement of IP3R2 in advanced stages of HF (30).

Prevention of RyR2 Posttranslational Modifications Attenuates Mitochondrial Dysfunction in HF. Mitochondrial ROS levels were markedly reduced in cardiomyocytes isolated from mCAT × RyR2-S2808D mice [mice expressing leaky RyR2 channels (RyR2-S2808D) crossed with mCAT mice] compared with RyR2-S2808D littermates, both in HF and sham conditions (Fig. 1*E*). Moreover, RyR2 oxidation and nitrosylation were significantly decreased in left ventricular samples from mCAT × RyR2-S2808D mice compared with RyR2-S2808D littermates (Fig. 2 *A*–*C*). SR Ca^{2+} leak (Fig. S2) and mitochondrial Ca^{2+} accumulation (Fig. 1 *A*–*D* and Fig. S1) observed in RyR2-S2808D were significantly reduced after crossing with mCAT mice. Additionally, post-MI, HF progression was markedly attenuated in mCAT × RyR2-S2808D mice (Fig. 2*G* and Table S1). These data show that mitochondria are a critical source of ROS that oxidizes RyR2 and promotes SR Ca^{2+} leak in failing hearts although there are likely additional sources of ROS, such as xanthine oxidase, that are significantly increased in failing hearts (Fig. S8).

Genetic ablation of the RyR2 PKA phosphorylation site at Ser^{2808} attenuated cardiac mitochondrial dysmorphology after MI (Fig. 3 *B* and *F*–*I*) and reduced mitochondrial ROS levels (Fig. 1*E*), indicating that, in addition to oxidation, PKA phosphorylation

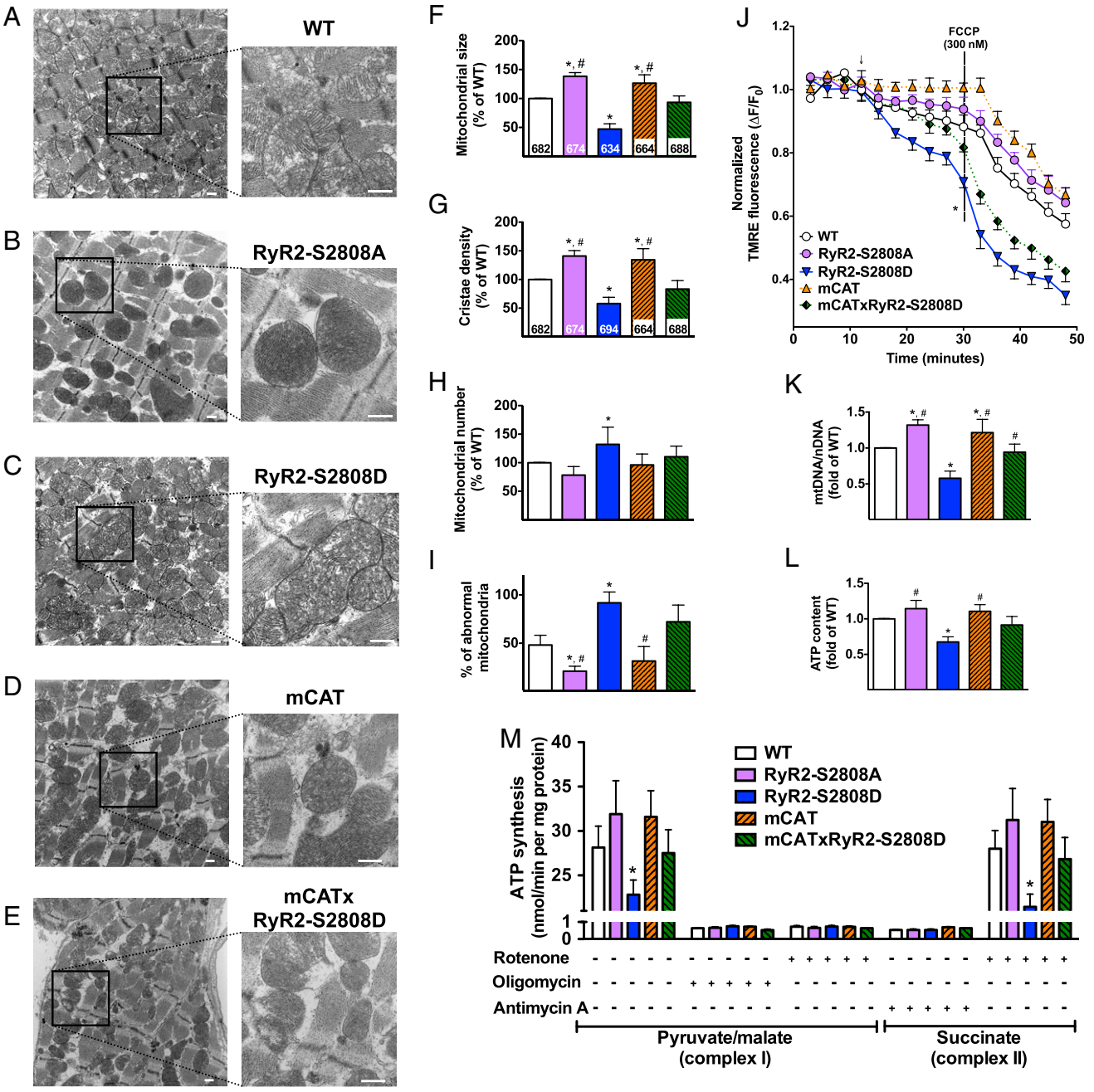

Fig. 3. Leaky RyR2 channels and mitochondrial dysfunction in heart failure. (*A–E*) Representative transmission electron micrographs of cardiac mitochondria post myocardial infarction from WT (*A*), RyR2-S2808A (no leak) (*B*), RyR2-S2808D (leaky) (*C*), mCAT (*D*), mCAT × RyR2-S2808D (*E*), $n = 5$ per group. (Magnification: *A–E*, 15,000×; *Insets*, 50,000×.) (Scale bars: 500 nm.) Note the diffuse myofibrillar disarray. (*F–I*) Quantification of ultrastructural mitochondrial alterations depicted in *A–E*. Mitochondrial size (*F*) and cristae density (*G*). Numbers in the bars indicate the number of mitochondria analyzed. Quantification of mitochondrial number per image (*H*) and percentage of abnormal mitochondria per image at 15,000× (*I*). Relative number of damaged mitochondria was quantified by blinded observers from 8 to 10 images from different fields. Data are shown as mean ± SEM, $^{*}P < 0.05$ vs. WT; $^{\#}P < 0.05$ vs. RyR2-S2808D, ANOVA, Tukey–Kramer post hoc test. (*J*) Assessment of the inner mitochondrial membrane potential ($\Delta\psi_m$); the arrow denotes addition of H_2O_2 (100 μM). FCCP, carbonylcyanide-p-trifluoro-methoxy-phenyl-hydrazone. The * indicates significant difference ($P < 0.05$, ANOVA repeated measures, Tukey–Kramer post hoc test) of the WT group ($n = 8$) compared with RyR2-S2808D ($n = 7$), mCAT × RyR2-S2808D ($n = 7$), and mCAT ($n = 6$), or between RyR2-S2808D and mCAT × RyR2-S2808D groups. (*K*) Mitochondrial DNA (mtDNA)/nuclear DNA (nDNA) copy number and (*L*) ATP content assessed in left ventricle ($n = 8$ per group). (*M*) Measurement of ATP synthesis rates in cardiac mitochondria isolated from failing hearts of the indicated groups. ATP synthesis was driven by complex I (pyruvate/malate, 5 mM) and complex II (succinate 5 mM). The specificity of the measurements was verified using inhibitors (0.5 μM) of respiratory complex, as indicated ($n = 3$ per group, triplicate measurements per sample). All data are shown as mean ± SEM, $^{*}P < 0.05$ vs. WT; $^{\#}P < 0.05$ vs. RyR2-S2808D, ANOVA, Tukey–Kramer post hoc test.

of RyR2 channel promotes SR Ca^{2+} leak and mitochondrial dysfunction. Indeed, RyR2-S2808A ventricular cardiomyocytes exhibited reduced mitochondrial Ca^{2+} uptake (Fig. 1 *B–D* and Fig. S1) and increased mtDNA levels (Fig. 3*K*). We also observed a trend toward ameliorated $\Delta\psi_m$ dissipation (Fig. 3*J*) and increased ATP content and synthesis (Fig. 3 *L* and *M*).

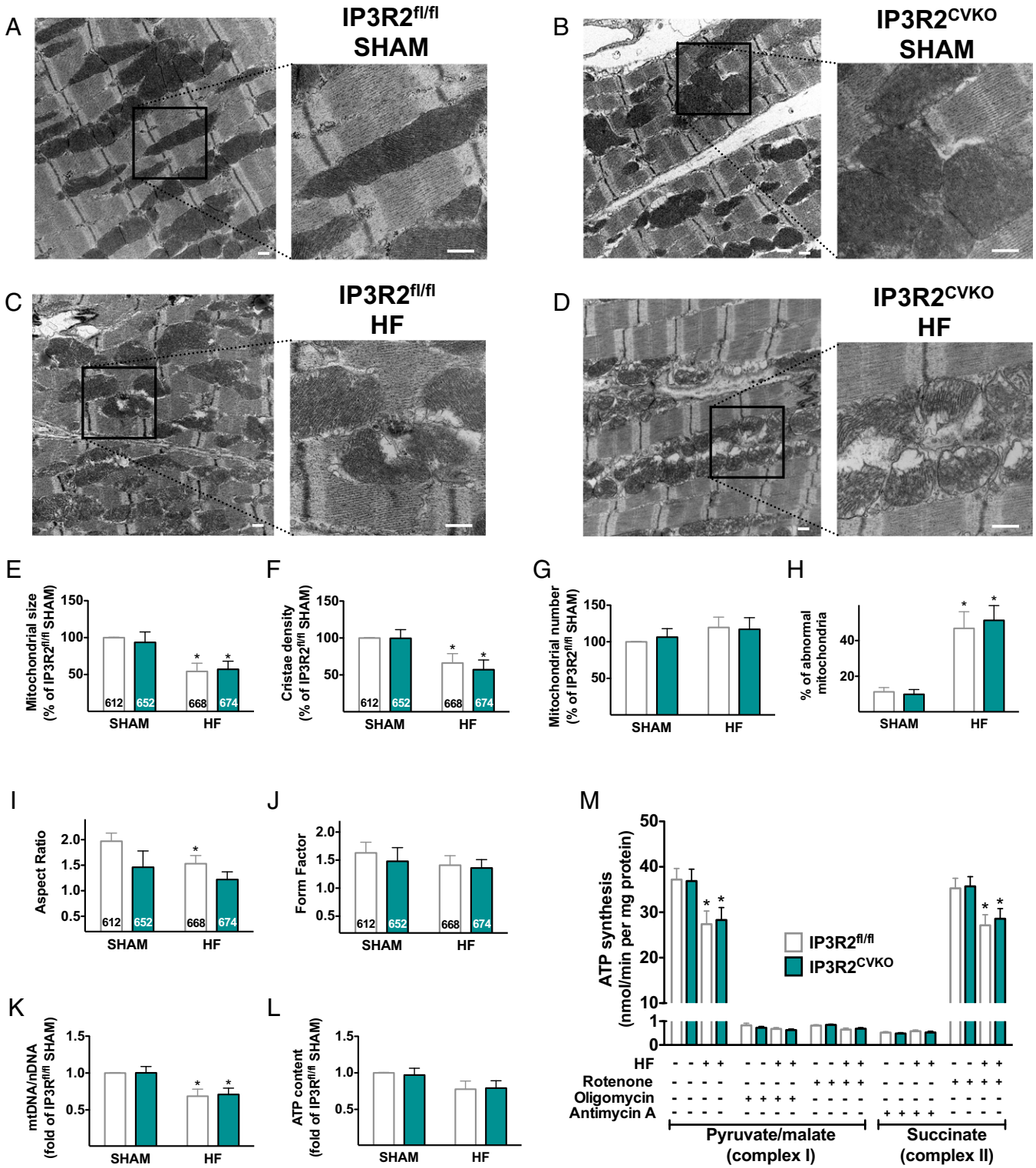

Fig. 4. Cardiac ablation of IP3R2 does not rescue mitochondrial abnormalities observed in failing hearts. (*A–D*) Representative transmission electron micrographs of cardiac mitochondria in SHAM conditions (*A* and *B*) and post myocardial infarction (*C* and *D*) from IP3R2$^{fl/fl}$ (*A* and *C*) and IP3R2^{CVKO} mice (*B* and *D*), $n = 5$ per group. (Magnification: *A–D*, 15,000×; *Insets*, 50,000×.) (Scale bars: 500 nm.) (*E–J*) Morphometric analysis of mitochondrial ultrastructure. Mitochondrial size (*E*) and cristae density (*F*). Quantification of mitochondrial number per image (*G*) and percentage of abnormal mitochondria per image at 15,000× (*H*). Evaluation of aspect ratio (*I*) and format form (*J*) (see *SI Materials and Methods* for details). (*K*) Mitochondrial DNA (mtDNA)/nuclear DNA (nDNA) copy number assessed in left ventricular tissue. (*L*) Assessment of ATP content in left ventricle ($n = 6$ per group) and (*M*) measurement of ATP synthesis rates in isolated mitochondria in sham conditions and 4 wk after coronary artery ligation, as described in Fig. 3*M*. All data are shown as mean ± SEM, $^*P < 0.05$ vs. SHAM; two-tailed *t* test. Numbers in the bars indicate the number of mitochondria analyzed.

RyR2-S2808A mice harboring nonleaky RyR2 channels exhibited reduced depletion of calstabin2 from the RyR2 complex in HF (Fig. 2 *A* and *F*), and significantly less RyR2 oxidation and nitrosylation (Fig. 2 *A*–*C*) and reduced post-MI HF progression (Fig. 2*G* and Table S1).

Taken together, our experimental findings demonstrate that SR Ca^{2+} leak via RyR2, but not IP3R2, channels plays a crucial role in the pathophysiology of mitochondrial Ca^{2+} overload and dysfunction in HF. Our data suggest a feedback loop between SR and mitochondria in HF in which SR Ca^{2+} leak triggers mitochondrial dysfunction and increases ROS production, which in turn can further oxidize RyR2 and enhance intracellular Ca^{2+} leak, contributing to impaired cardiac function post-MI.

Materials and Methods

The targeted deletion of IP3R2 in ventricular cardiomyocytes was obtained by flanking exon 3 of *IP3R2* with loxP sites (Fig. S2). Mice harboring the $IP3R2^{flox/flox}$ allele were bred with MHC-Cre transgenic mice to obtain a cardiac ventricular-specific ablation of IP3R2. A detailed description of materials and methods for in vivo experiments (31–35), isolation of adult cardiomyocytes (34, 36), isolation of mitochondria (37), assessment of mitochondrial dynamics, Ca^{2+} content, and membrane potential (34, 37), real-time RT-qPCR (38, 39), immunoprecipitation/immunoblot, and electron microscopy (40) can be found in *SI Materials and Methods*.

Ethical Approval. All studies were performed according to protocols approved by the Institutional Animal Care and Use Committee (IACUC) of Columbia University.

Statistics. All results are presented as mean ± SEM. Statistical analysis was performed using an unpaired two-tailed *t* test (for two groups) and one-way ANOVA with Tukey–Kramer post hoc test (for groups of three or more) unless otherwise indicated. *P* values of less than 0.05 were considered significant.

ACKNOWLEDGMENTS. We are grateful to Bi-Xing Chen, Qi Yuan, and Jingyi Yang (Columbia University) for technical support, Alain Lacampagne and Jeremy Fauconnier (INSERM and University of Montpellier) for critical discussion and helpful assistance, and Peter S. Rabinovitch (University of Washington) for providing the mCAT mouse founders. This work was supported by American Heart Association Grants 13POST16810041 and 15SDG25300007 (to G.S.), NIH Grant R01HL061503, and the Leducq Foundation (to A.R.M.).

1. Santulli G, Marks AR (2015) Essential roles of intracellular calcium release channels in muscle, brain, metabolism, and aging. *Curr Mol Pharmacol*, in press.
2. Marks AR (2013) Calcium cycling proteins and heart failure: Mechanisms and therapeutics. *J Clin Invest* 123(1):46–52.
3. Moschella MC, Marks AR (1993) Inositol 1,4,5-trisphosphate receptor expression in cardiac myocytes. *J Cell Biol* 120(5):1137–1146.
4. Ventura-Clapier R, Garnier A, Veksler V (2004) Energy metabolism in heart failure. *J Physiol* 555(Pt 1):1–13.
5. Whelan RS, et al. (2012) Bax regulates primary necrosis through mitochondrial dynamics. *Proc Natl Acad Sci USA* 109(17):6566–6571.
6. Nickel A, Löffler J, Maack C (2013) Myocardial energetics in heart failure. *Basic Res Cardiol* 108(4):358.
7. Huss JM, Kelly DP (2005) Mitochondrial energy metabolism in heart failure: A question of balance. *J Clin Invest* 115(3):547–555.
8. Drago I, De Stefani D, Rizzuto R, Pozzan T (2012) Mitochondrial Ca^{2+} uptake contributes to buffering cytoplasmic Ca^{2+} peaks in cardiomyocytes. *Proc Natl Acad Sci USA* 109(32):12986–12991.
9. García-Rivas G de J, Carvajal K, Correa F, Zazueta C (2006) Ru360, a specific mitochondrial calcium uptake inhibitor, improves cardiac post-ischaemic functional recovery in rats in vivo. *Br J Pharmacol* 149(7):829–837.
10. O-Uchi J, et al. (2014) Adrenergic signaling regulates mitochondrial Ca^{2+} uptake through Pyk2-dependent tyrosine phosphorylation of the mitochondrial Ca^{2+} uniporter. *Antioxid Redox Signal* 21(6):863–879.
11. Holmström KM, et al. (2015) Assessment of cardiac function in mice lacking the mitochondrial calcium uniporter. *J Mol Cell Cardiol* 85:178–182.
12. Paillard M, et al. (2013) Depressing mitochondria-reticulum interactions protects cardiomyocytes from lethal hypoxia-reoxygenation injury. *Circulation* 128(14):1555–1565.
13. Elrod JW, et al. (2010) Cyclophilin D controls mitochondrial pore-dependent Ca^{2+} exchange, metabolic flexibility, and propensity for heart failure in mice. *J Clin Invest* 120(10):3680–3687.
14. Odagiri K, et al. (2009) Local control of mitochondrial membrane potential, permeability transition pore and reactive oxygen species by calcium and calmodulin in rat ventricular myocytes. *J Mol Cell Cardiol* 46(6):989–997.
15. Ishida H, et al. (2004) Nicorandil attenuates the mitochondrial Ca^{2+} overload with accompanying depolarization of the mitochondrial membrane in the heart. *Naunyn Schmiedebergs Arch Pharmacol* 369(2):192–197.
16. Tocchetti CG, et al. (2011) Playing with cardiac "redox switches": The "HNO way" to modulate cardiac function. *Antioxid Redox Signal* 14(9):1687–1698.
17. Griffiths EJ, Balaska D, Cheng WH (2010) The ups and downs of mitochondrial calcium signalling in the heart. *Biochim Biophys Acta* 1797(6-7):856–864.
18. Gong G, Liu X, Wang W (2014) Regulation of metabolism in individual mitochondria during excitation-contraction coupling. *J Mol Cell Cardiol* 76:235–246.
19. Hoffman NE, et al. (2015) Ca^{2+} entry via Trpm2 is essential for cardiac myocyte bioenergetics maintenance. *Am J Physiol Heart Circ Physiol* 308(6):H637–H650.
20. Balaban RS, Bose S, French SA, Territo PR (2003) Role of calcium in metabolic signaling between cardiac sarcoplasmic reticulum and mitochondria in vitro. *Am J Physiol Cell Physiol* 284(2):C285–C293.
21. Rizzuto R, Duchen MR, Pozzan T (2004) Flirting in little space: The ER/mitochondria Ca^{2+} liaison. *Sci STKE* 2004(215):re1.
22. Min CK, et al. (2012) Coupling of ryanodine receptor 2 and voltage-dependent anion channel 2 is essential for Ca^{2+} transfer from the sarcoplasmic reticulum to the mitochondria in the heart. *Biochem J* 447(3):371–379.
23. Lehnart SE, et al. (2005) Phosphodiesterase 4D deficiency in the ryanodine-receptor complex promotes heart failure and arrhythmias. *Cell* 123(1):25–35.
24. Yuan Q, et al. (2014) Functional role of Calstabin2 in age-related cardiac alterations. *Sci Rep* 4:7425.
25. Sciarretta S, et al. (2015) Role of NADPH oxidase in the regulation of autophagy in cardiomyocytes. *Clin Sci (Lond)* 128(7):387–403.
26. Kaludercic N, Deshwal S, Di Lisa F (2014) Reactive oxygen species and redox compartmentalization. *Front Physiol* 5:285.
27. Takimoto E, et al. (2005) Oxidant stress from nitric oxide synthase-3 uncoupling stimulates cardiac pathologic remodeling from chronic pressure load. *J Clin Invest* 115(5):1221–1231.
28. Chalmers S, McCarron JG (2008) The mitochondrial membrane potential and Ca^{2+} oscillations in smooth muscle. *J Cell Sci* 121(Pt 1):75–85.
29. Pitt GS, Dun W, Boyden PA (2006) Remodeled cardiac calcium channels. *J Mol Cell Cardiol* 41(3):373–388.
30. Go LO, et al. (1995) Differential regulation of two types of intracellular calcium release channels during end-stage heart failure. *J Clin Invest* 95(2):888–894.
31. Schriner SE, et al. (2005) Extension of murine life span by overexpression of catalase targeted to mitochondria. *Science* 308(5730):1909–1911.
32. Santulli G, et al. (2012) CaMK4 gene deletion induces hypertension. *J Am Heart Assoc* 1(4):e001081.
33. Shan J, et al. (2010) Phosphorylation of the ryanodine receptor mediates the cardiac fight or flight response in mice. *J Clin Invest* 120(12):4388–4398.
34. Xie W, et al. (2015) Mitochondrial oxidative stress promotes atrial fibrillation. *Sci Rep* 2015(5):11427.
35. Umanskaya A, et al. (2014) Genetically enhancing mitochondrial antioxidant activity improves muscle function in aging. *Proc Natl Acad Sci USA* 111(42):15250–15255.
36. Xie W, et al. (2013) Imaging atrial arrhythmic intracellular calcium in intact heart. *J Mol Cell Cardiol* 64:120–123.
37. Fusco A, et al. (2012) Mitochondrial localization unveils a novel role for GRK2 in organelle biogenesis. *Cell Signal* 24(2):468–475.
38. Santulli G, et al. (2014) A selective microRNA-based strategy inhibits restenosis while preserving endothelial function. *J Clin Invest* 124(9):4102–4114.
39. Sorriento D, et al. (2010) Intracardiac injection of AdGRK5-NT reduces left ventricular hypertrophy by inhibiting NF-kappaB-dependent hypertrophic gene expression. *Hypertension* 56(4):696–704.
40. Santulli G, et al. (2015) Calcium release channel RyR2 regulates insulin release and glucose homeostasis. *J Clin Invest* 125(5):1968–1978.

Supporting Information

Santulli et al. 10.1073/pnas.1513047112

SI Materials and Methods

Targeted Deletion of IP3R2 in Ventricular Cardiomyocytes. Exon 3 of IP3R2 was targeted by flanking it with loxP sites (Fig. S2). Mice harboring the $IP3R2^{flox/flox}$ allele ($IP3R2^{fl/fl}$) were bred with MHC-Cre transgenic mice to obtain a cardiac ventricular-specific ablation of IP3R2 ($IP3R2^{CVKO}$). Genotypes were verified by PCR (Fig. S2 and Table S2). Generation of mCAT, RyR2-S2808D, and RyR2-S2808A mice has been described (1, 31, 33). All mice were backcrossed into the C57BL/6 background for >10 generations. All animal studies were performed according to protocols approved by the Institutional Animal Care and Use Committee (IACUC) and according to NIH guidelines. All in vivo and in vitro experiments were conducted on male mice by operators who were blinded to the genotypes of the animals. No samples, mice, or data points were excluded from the reported analyses.

In Vivo Experiments. Transthoracic 2D echocardiography was performed using a 12-MHz probe (VeVo; Visualsonics). M-mode interrogation was performed in the parasternal short-axis view. Left ventricular (LV) end-diastolic and end-systolic dimensions and septal and posterior wall thicknesses were determined and used to calculate fractional shortening and ejection fractions (32). After baseline echocardiography, permanent occlusion of the proximal left anterior descending (LAD) coronary artery was performed in 5-mo-old mice. A small (1.5-cm) left thoracotomy was performed via the fourth intercostal space, and the lungs were retracted to expose the heart. After opening the pericardium, the LAD coronary artery was located and ligated with 8-0 silk suture near its origin between the pulmonary outflow tract and the edge of the left atrium, 2 mm lower than the tip of the left auricle. The ligation was deemed successful when the anterior wall of the LV turned pale. Animals were kept on a heating pad until they recovered. The group of mice undergoing sham ligation had a similar surgical procedure without tightening the suture around the artery. Echocardiography was repeated at 1, 2, and 4 wk post-MI. Serum concentration of troponin I was measured 1 d after coronary artery ligation using a commercially available immunoassay kit to indirectly estimate myocardial infarct size. Infarct area was also assessed in a distinct group of animals using 2-3-5-triphenyltetrazolium chloride and expressed as percentage of total LV area. Blood pressure and cardiac contractility were measured as described (32).

Isolation of Adult Cardiomyocytes and Measurement of Ca^{2+} and Mitochondrial Membrane Potential. The hearts were excised and washed in Ca^{2+}-free Tyrode solution, followed by retrograde perfusion with buffer containing collagenase II (Worthington Biochemical Corporation) at 37 °C for 10 min. The LV was subsequently dissociated into single myocytes, and extracellular Ca^{2+} concentration was progressively increased to reach a final concentration of 1.8 mM. Cardiomyocytes were plated on glass coverslips coated with laminin (Thermo Fisher Scientific). To determine intracellular [Ca^{2+}], cardiomyocytes were loaded with 5 μM Fluo-4 acetoxymethyl (AM) ester (Thermo Fisher Scientific) for 20 min and washed three times with dye-free Tyrode solution. Ca^{2+} sparks were recorded using a Zeiss LSM 5 Live confocal microscope in line scan mode. The fluorophore was excited with an argon laser at 488 nm, and emission was recorded at 505–530 nm. Ca^{2+} sparks were quantified using a software algorithm (IDL; ITT Visual Information Solutions) and calculated as sparks/100 μm/s (34–36). Dynamic mitochondrial Ca^{2+} was evaluated in enzymatically isolated cardiomyocytes incubated with Rhod2-AM (2 μm; Thermo Fisher Scientific) for 1 h at 37 °C and then washed for deesterification. After loading, the cells were placed on the stage of a Zeiss LSM 5 Live confocal microscope (63× oil immersion lens) where Rhod2 fluorescence signals were recorded by excitation at 561 nm and measurement of the emitted light at 588 nm. Cardiomyocytes were stimulated by pacing (3 Hz) or pharmacologically triggering Ca^{2+} leak via RyR2 using FK506 (5 μM).

To assess mitochondrial ROS levels, isolated cardiomyocytes were incubated for 20 min with the mitochondria-targeted fluorescent indicator of superoxide production MitoSOX Red (5 μM; Thermo Fisher Scientific) and washed. Using a confocal laser-scanning microscope (Zeiss LSM 5 Live, 40× oil immersion lens), MitoSOX Red fluorescence was excited at 488 nm, and the emitted signal was filtered through a band pass filter (540–625 nm). The scanned parameters were fixed for all scans. For each group, fluorescence intensities of >100 cells randomly selected from several different dishes were examined.

To measure mitochondrial membrane potential ($\Delta\psi_m$), cardiomyocytes were incubated with the fluorescent indicator tetramethylrhodamine ethyl ester (TMRE; 30 nM; Thermo Fisher Scientific) for 20 min. TMRE fluorescence was excited at 532 nm, and the emitted signal was collected through a band pass filter (540–625 nm, Zeiss LSM 5 Live, 40× oil immersion lens). To minimize the impact of subcellular variability on $\Delta\psi_m$, TMRE fluorescence was measured in five different areas in each cell. At the end of each experiment, cells were exposed to the mitochondrial uncoupler carbonylcyanide-p-trifluoro-methoxyphenyl-hydrazone (FCCP, 300 nM). Images were obtained every 5 min, and fluorescence signals were normalized to the fluorescence measured at the start of the experiment.

Isolation of Cardiac Mitochondria. Murine cardiac mitochondria were isolated using previous established procedures (11, 13, 37). In brief, mice were euthanized, and the heart was excised. The LV was minced on ice, resuspended, and homogenized in 1.5 mL of buffer (10 mM Tris, 250 mM sucrose, 1× protease inhibitor mixture, pH 7.4) supplemented with 1 mM EDTA. Homogenates were centrifuged at 1,000 × *g* for 5 min at 4 °C (pellet discarded and supernatant recentrifuged at 500 × *g*). The supernatant was centrifuged at 10,000 × *g* for 15 min to pellet the mitochondria. The pellet was then resuspended in the homogenization buffer (without EDTA) and used for experiments within 1 h. All steps were performed at 4 °C. ATP synthesis rates in isolated cardiac mitochondria were determined using a bioluminescence kit (Sigma-Aldrich), according to the manufacturer's instructions. Briefly, 10 μg of cardiac mitochondria were dissolved in 50 μL of buffer (10 mM Hepes, 125 mM KCl, 5 mM $MgCl_2$, 2 mM K_2HPO_4, pH 7.42) to determine complex I (5 mM pyruvate/malate) or complex II (5 mM succinate) driven ATP synthesis. To determine the rates of nonmitochondrial ATP production, measurements with substrates were repeated in the presence (0.5 μM) of inhibitors of respiratory complex: rotenone (complex I), antimycin (complex III), and oligomycin (complex IV). To avoid the reverse electron transfer effect, succinate-driven ATP synthesis was assessed in the presence of rotenone (0.5 μM). ATP content in the LV was determined as described (37). The endogenous mitochondrial Ca^{2+} content was measured in cardiac mitochondria isolated as reported above, except that all buffers were EGTA/EDTA-free to avoid chelating Ca^{2+}. Isolated mitochondrial pellets were repeatedly washed

in buffers, resuspended in 0.6 M HCl, and sonicated (2 × 10 s at 40% of maximal power output). Absolute Ca^{2+} content (expressed as nmoles/mg protein) was determined using the *o*-cresolphthalein complexone assay (Cayman Chemical), according to the manufacturer's instructions.

Real-Time Quantitative Reverse Transcription PCR. Total RNA was isolated using TRIzol reagent (Thermo Fisher Scientific) in combination with the RNeasy Mini kit (Qiagen) followed by DNase treatment (38, 39), and cDNA was synthesized by means of a Thermo-Script RT-PCR System (Thermo Fisher Scientific), following the manufacturer's instructions. After reverse transcription, real-time quantitative PCR was performed in triplicate using the SYBR Green RT-PCR master mix kit and quantified by built-in SYBR Green Analysis (Thermo Fisher Scientific) (39, 40). To determine mitochondrial and nuclear DNA copy number (mtDNA and nDNA, respectively), a quantitative RT-qPCR was performed on 30 ng of total left ventricular DNA in each qPCR reaction using primer pairs for mitochondrial and genomic loci. Two different primer pairs were used to quantify and confirm relative mitochondrial (mt)/nuclear (n) DNA ratio: 12S and 16S for mtDNA, H19 and 18S for nDNA. Samples were measured in triplicate, and results were confirmed by at least three independent experiments. All of the primer sequences (Sigma-Aldrich) for gene analysis are listed in Table S2.

Immunoprecipitation/Immunoblot Analysis. Left ventricular samples were incubated with specific antibodies and protein A Sepharose beads (Amersham Pharmacia Biotech Inc.) at 4 °C for 2.5 h, and the beads were then washed. Immunoprecipitates were size-fractionated on SDS/PAGE gels (6% for RyR2 and IP3R2, 15% for calstabin2) and transferred onto nitrocellulose membranes for 2 h at 200 mA. To determine channel oxidation, the carbonyl groups in the protein side chains in the immunoprecipitated material were derivatized to 2,4-dinitrophenylhydrazone (2,4 DNPH) by reaction with 2,4-dinitrophenylhydrazine. The 2,4 DNPH signal was determined using a specific antibody, according to the manufacturer's instructions (Millipore). Anti-*S*-nitrosocysteine (anti-CysNO) antibody was purchased from Sigma-Aldrich. All immunoblots were developed with the Odyssey system (LI-COR Biosciences), using infrared-labeled anti-mouse and anti-rabbit IgG (1:10,000 dilution) secondary antibodies (40). The intensity of the bands was quantified by using the LI-COR Image Studio Software (LI-COR Biosciences).

Transmission Electron Microscopy. Cardiac left ventricles were fixed in 2.5% glutaraldehyde in 0.1 M Sørensen's buffer and postfixed in 1% OsO_4. After dehydration, samples were embedded in Lx-112 (Ladd Research Industries). After cutting (ultramicrotome MT-7000), 60-nm sections were stained with uranyl acetate and lead citrate and visualized (JEM-1200 EXII; JEOL). Eight to ten randomly taken sections for each animal were examined for morphological analyses, performed using Fiji software. Mitochondrial aspect ratio (major axis/minor axis) and form factor (perimeter^2/4π × area) were also measured. To estimate mitochondrial size and cristae density, a computerized point grid was digitally layered over the micrographic images. The densities of dots on the point grid were quantified as previously described (40). All of the analyses were performed in a blinded fashion.

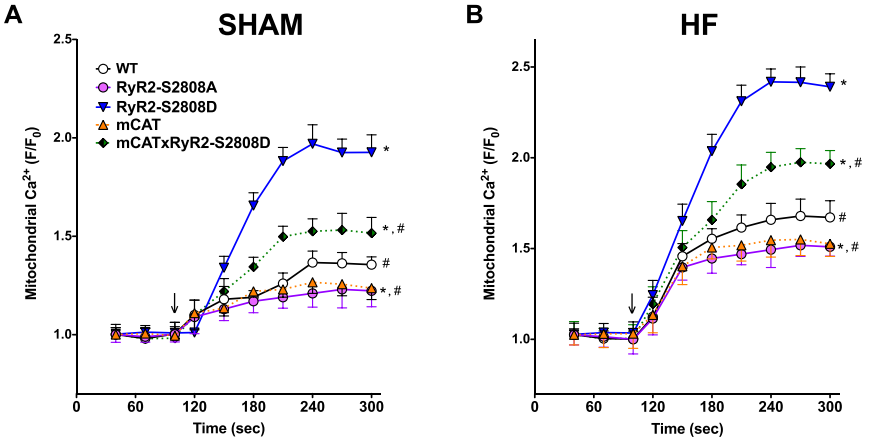

Fig. S1. Mitochondrial Ca^{2+} dynamics in isolated cardiomyocytes following pharmacologically triggered intracellular Ca^{2+} leak via RyR2. (*A* and *B*) Mitochondrial Ca^{2+} in response to FK506 (5 μM, arrow) was evaluated in cardiomyocytes (n = 20–35) enzymatically isolated from at least seven mice per group in SHAM (*A*) and HF (*B*) conditions. Data are shown as mean ± SEM; $^{*}P < 0.05$ vs. WT; $^{\#}P < 0.05$ vs. RyR2-S2808D; ANOVA repeated measures.

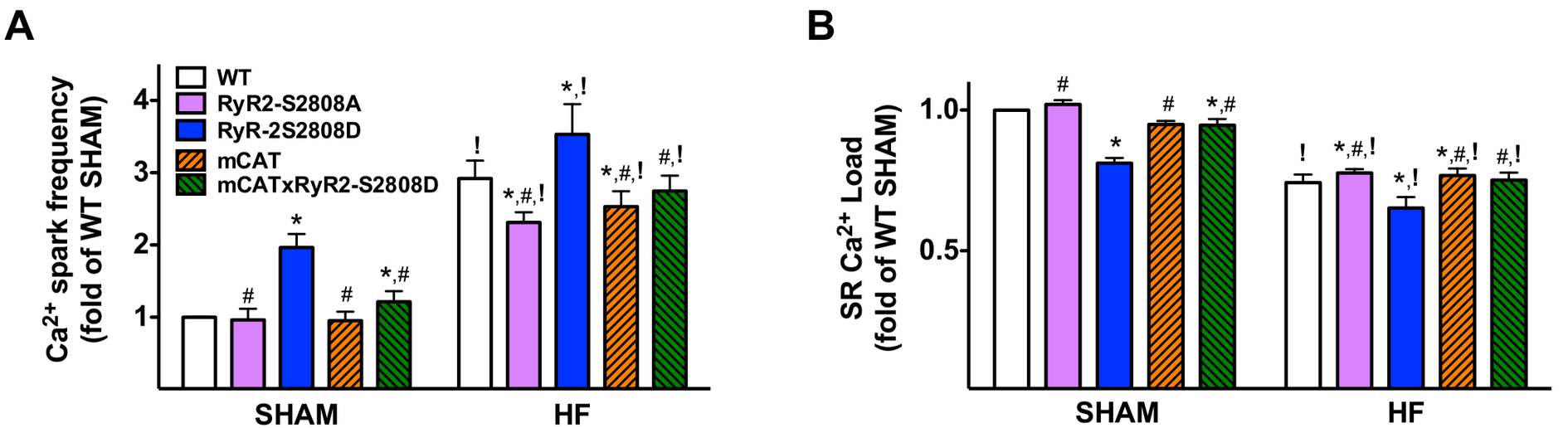

Fig. S2. Evaluation of intracellular Ca^{2+} leak in ventricular cardiomyocytes. (*A*) Average Ca^{2+} spark activity and (*B*) SR Ca^{2+} load, in ventricular cardiomyocytes ($n = 20$~22 cells per condition) enzymatically isolated from at least seven mice/group in SHAM and HF conditions. Data are shown as mean ± SEM, $^{*}P < 0.05$ vs. WT; $^{\#}P < 0.05$ vs. RyR2-S2808D, ANOVA, Tukey–Kramer post hoc test; $^{!}P < 0.05$ vs. SHAM, two-tailed *t* test.

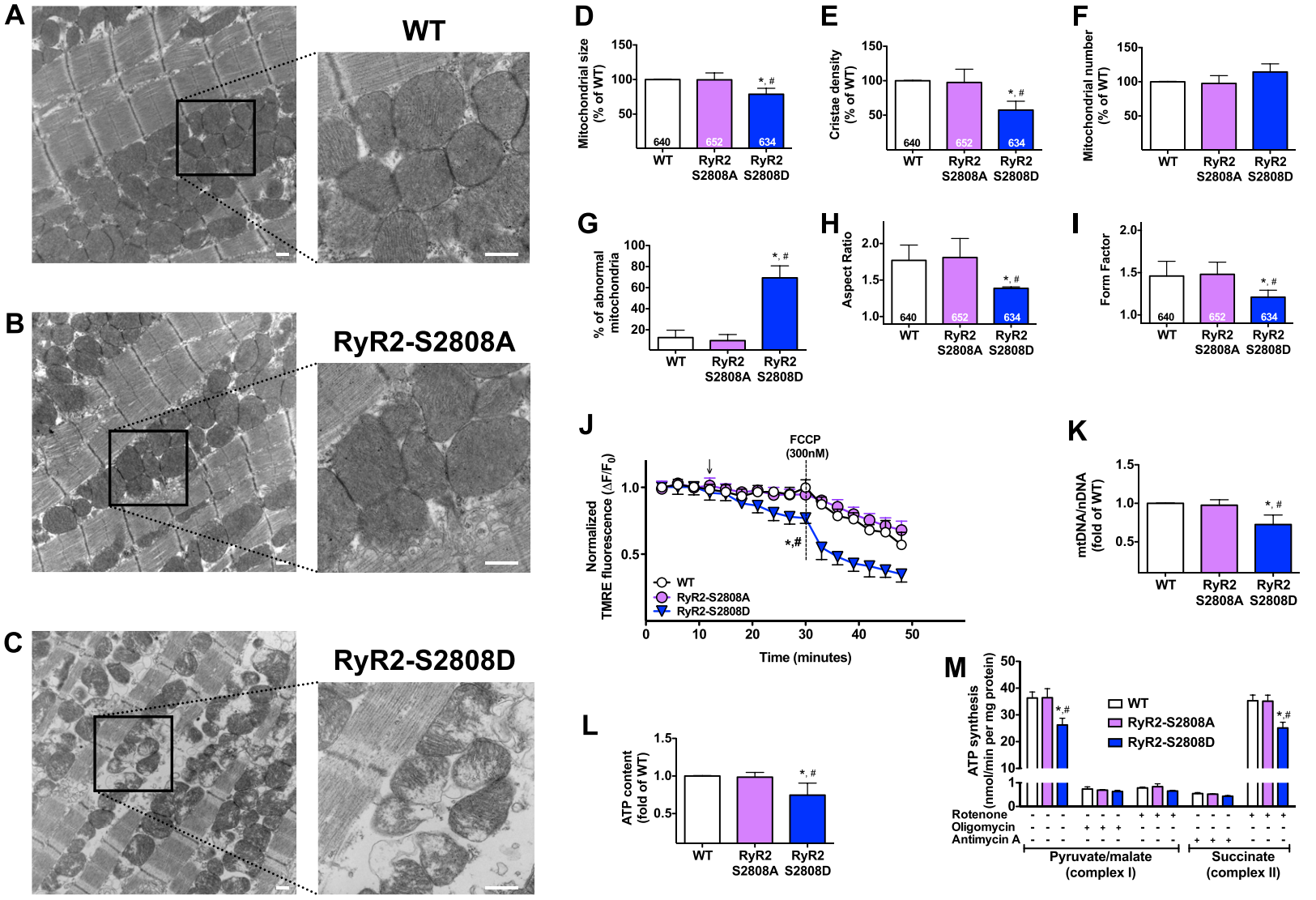

Fig. S3. Cardiac mitochondrial abnormalities and intracellular Ca^{2+} leak. (*A–C*) Representative transmission electron micrographs of cardiac mitochondria from 6-mo-old WT (*A*), RyR2-S2808A (*B*), and RyR2-S2808D (*C*), $n \geq 5$ per group. (Magnification: *A–C*, 15,000×; *Insets*, 50,000×.) (Scale bars: 500 nm.) (*D–I*) Morphometric analyses of mitochondria show abnormalities in RyR2-S2808D mice with leaky RyR2 channels. Mitochondrial size (*D*) and cristae density (*E*). Numbers in the bars indicate the number of mitochondria analyzed. Quantification of mitochondrial number per image (*F*) and percentage of abnormal mitochondria per image at 15,000× (*G*); mitochondria were defined as abnormal when a loss of electron density was detectable in more than 20% of the area of a mitochondrion. Aspect ratio (*H*) and form factor (*I*), See *SI Materials and Methods* for details. (*J–M*) Evaluation of mitochondrial function. Assessment of mitochondrial membrane potential ($\Delta\psi_m$, *J*); the arrow denotes addition of H_2O_2 (100 μM); FCCP, carbonylcyanide-p-trifluoro-methoxy-phenyl-hydrazone; the * indicates significant difference ($P < 0.05$, ANOVA repeated measures, Tukey–Kramer post hoc test) between the RyR2-S2808D group ($n = 8$) compared with WT ($n = 9$) and to RyR2-S2808A ($n = 8$). Mitochondrial DNA (mtDNA)/nuclear DNA (nDNA) copy number was assessed in left ventricular samples (*K*). Measurement of ATP content in left ventricle (*L*, $n = 8$ per group) and ATP synthesis rates in isolated cardiac mitochondria (*M*) driven by complex I (pyruvate/malate, 5 mM) and complex II (succinate 5 mM). The specificity of the measurements was verified using inhibitors (0.5 μM) of the respiratory complex, as indicated ($n = 5$ per group, triplicate measurements per sample). Data are shown as mean ± SEM, $^*P < 0.05$ vs. WT; $^{\#}P < 0.05$ vs. RyR2-S2808A.

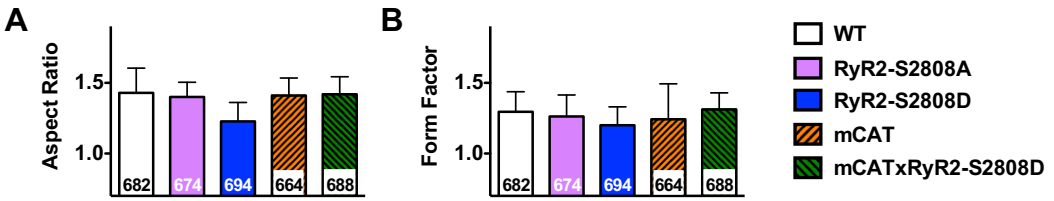

Fig. S4. Assessment of mitochondrial morphological dynamism in HF. (*A*) Aspect ratio and (*B*) form factor were measured as described in *SI Materials and Methods* in cardiac mitochondria from 6-mo-old WT, RyR2-S2808A, RyR2-S2808D, mCAT, and mCAT × RyR2-S2808D mice, 4 wk after myocardial infarction; $n \geq 5$ per group; see also Fig. 3 *A*–*E*. All data are shown as mean ± SEM; numbers in the bars indicate the number of mitochondria analyzed.

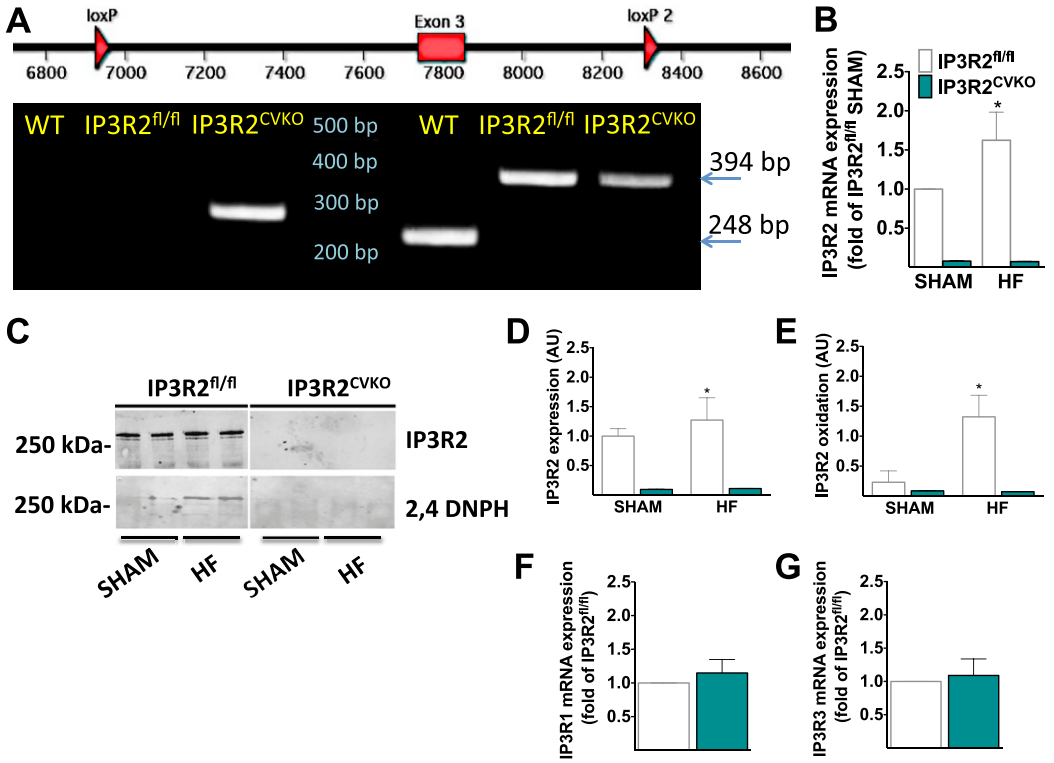

Fig. S5. Generation of cardiac specific ablation of IP3R2. (*A*) Schematic illustration of the generation of the IP3R2 floxed mouse (*Top*) and representative PCR for the genotype detection of WT, IP3R2$^{fl/fl}$, and IP3R2KO mice. (*B*) Determination of IP3R2 mRNA levels by real time quantitative reverse transcription PCR (RT-qPCR) analysis of total RNA from isolated cardiomyocytes, using actin as internal standard; each bar represents mean ± SEM of four independent experiments, in each of which reactions were performed in triplicate using the pooled total RNAs from five mice per group. (*C*) IP3R2 from isolated ventricular cardiomyocytes was immunoprecipitated and immunoblotted. 2,4 DNPH, 2,4-dinitrophenylhydrazone. (*D* and *E*) Quantification of data shown in *C*. Data shown represent means ± SEM from triplicate experiments. *$P < 0.05$ vs. IP3R2$^{fl/fl}$, two-tailed *t* test. (*F* and *G*) Levels of IP3R isoforms after cardiac-specific ablation of IP3R2. Determination of IP3R1 (*F*) and IP3R3 (*G*) mRNA levels by RT-qPCR analysis of total RNA from isolated cardiomyocytes, using actin as internal standard; each bar represents mean ± SEM of four independent experiments, in each of which reactions were performed in triplicate using the pooled total RNAs from five mice/group.

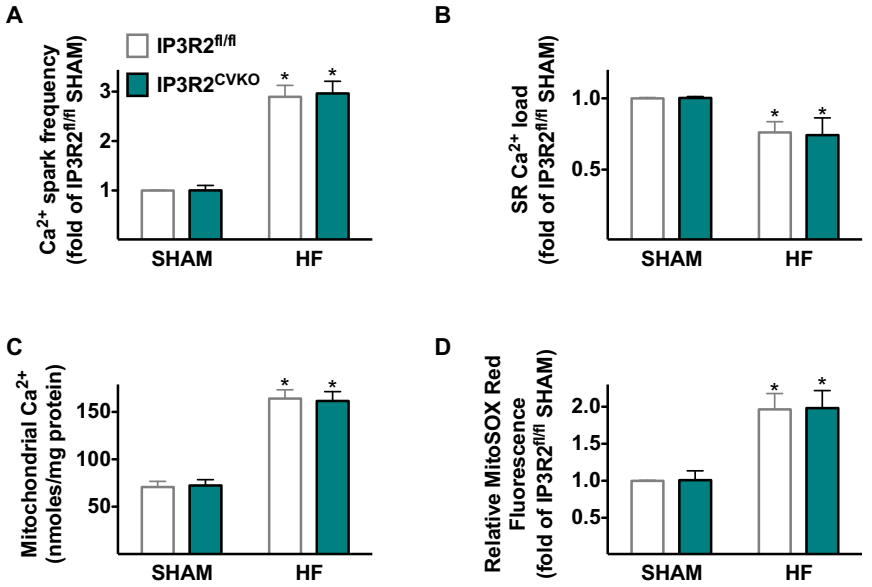

Fig. S6. Effects of cardiac ablation of IP3R2 on Ca^{2+} spark frequency, SR Ca^{2+} load, mitochondrial Ca^{2+} content, and ROS production. (*A*) Average Ca^{2+} spark frequency, (*B*) SR Ca^{2+} load, and (*C*) mitochondrial Ca^{2+} in ventricular cardiomyocytes (n = 20∼22 cells) isolated from at least six mice per group in SHAM and HF conditions. Data are shown as mean ± SEM. (*D*) Evaluation of mitochondrial ROS generation in ventricular cardiomyocytes using the mitochondria-targeted fluorescent indicator of superoxide production MitoSOX Red. n > 100 ventricular myocytes from at least four mice in each group. AU, arbitrary units. Data are shown as mean ± SEM, *P < 0.05 vs. WT; one-way ANOVA, Tukey–Kramer post hoc test.

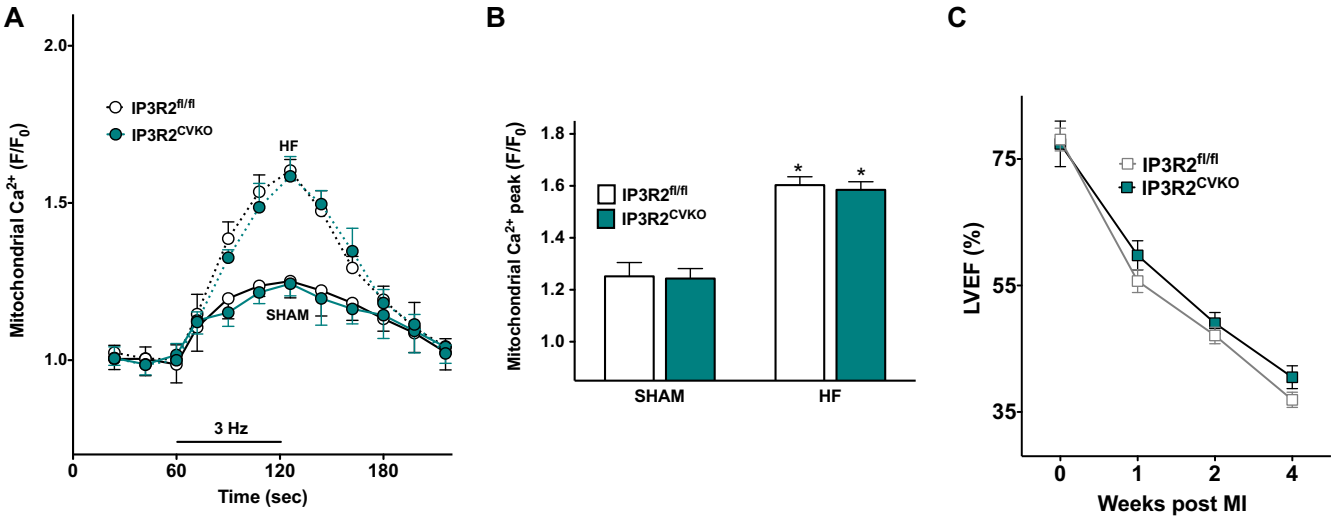

Fig. S7. Effects of cardiac ablation of IP3R2 on mitochondrial Ca^{2+} dynamics and HF progression after myocoardial infarction. (*A*) Mitochondrial Ca^{2+} in response to 3 Hz stimulation was evaluated in cardiomyocytes (n = 25–30) enzymatically isolated from at least seven mice per group in SHAM (solid lines) and HF (dotted lines) conditions. (*B*) The mitochondrial Ca^{2+} peak. Data are shown as means ± SEM, *P < 0.05 vs. SHAM, two-tailed t test. (*C*) Progressive cardiac dysfunction after left anterior coronary artery ligation assessed by serial ultrasound in $IP3R2^{fl/fl}$ and $IP3R2^{CVKO}$. LVEF, left ventricular ejection fraction; n = 16–18 per group. See also Table S1.

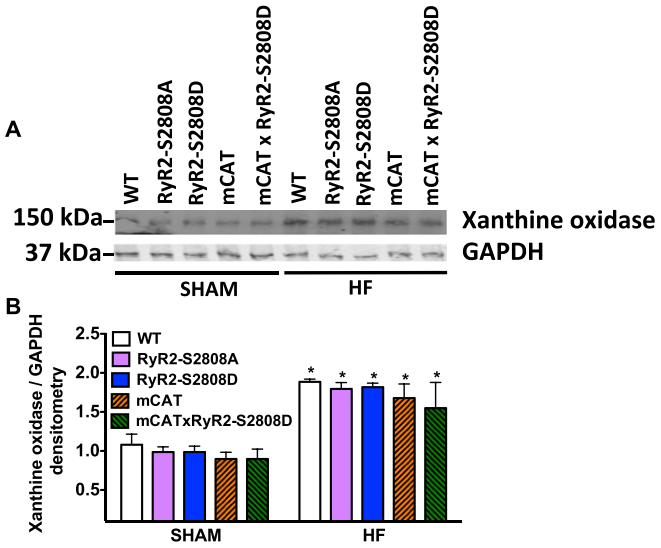

Fig. S8. Xanthine oxidase expression is increased in failing hearts, and in vivo genetic enhancement of mitochondrial antioxidant activity does not prevent such increase. (*A*) Representative immunoblots showing xanthine oxidase levels in cardiomyocytes enzymatically isolated from at least seven mice per group in SHAM and HF conditions. GAPDH was used as loading control. (*B*) Densitometry quantification from triplicate experiments; data are shown as mean ± SEM, **P* < 0.05 vs. SHAM.

Table S1. Characteristics of 6-mo-old SHAM and HF (post-MI) mice

Characteristic	WT	RyR2-S2808A	RyR2-S2808D	mCAT	mCATx RyR2-S2808D	IP3R2$^{fl/fl}$	IP3R2^{CVKO}
SHAM							
BW, g	25.4 ± 0.8	26.1 ± 1.1	25.1 ± 1.1	25.8 ± 1.1	25.2 ± 0.9	26.2 ± 0.9	26.5 ± 1.1
HR, bpm	506 ± 46	496 ± 52	492 ± 48	490 ± 54	498 ± 42	502 ± 46	482 ± 56
HW/BW, mg/g	4.8 ± 0.5	4.9 ± 0.4	5.2 ± 0.5	4.7 ± 0.4	5.1 ± 0.5	4.9 ± 0.5	4.8 ± 0.3
LW/BW, mg/g	5.4 ± 0.4	5.3 ± 0.3	5.8 ± 0.4	5.3 ± 0.4	5.5 ± 0.4	5.3 ± 0.4	5.4 ± 0.5
EF, %	78.08 ± 1.1$^{\#}$	78.26 ± 1.2$^{\#}$	60.26 ± 0.9*	78.68 ± 1.1$^{\#}$	67.18 ± 1.1*,$^{\#}$	78.32 ± 1.2$^{\#}$	77.14 ± 1.1$^{\#}$
FS, %	51.11 ± 1.1$^{\#}$	50.92 ± 1.1$^{\#}$	31.76 ± 0.8*	51.18 ± 0.9$^{\#}$	35.94 ± 0.7*,$^{\#}$	51.66 ± 1.1$^{\#}$	50.78 ± 0.9$^{\#}$
DBP, mmHg	80.12 ± 2.4	81.1 ± 2.7	80.11 ± 2.1	80.22 ± 2.1	79.8 ± 2.2	82.34 ± 2.7	81.9 ± 2.9
dP/dt$_{max}$, mmHg/s	7685 ± 522$^{\#}$	7849 ± 535$^{\#}$	6702 ± 392*	7689 ± 593$^{\#}$	7115 ± 514*,$^{\#}$	7724 ± 536$^{\#}$	7692 ± 544$^{\#}$
dP/dt$_{min}$, mmHg/s	6125 ± 415$^{\#}$	6214 ± 488$^{\#}$	5055 ± 495*	6152 ± 501$^{\#}$	5568 ± 487*,$^{\#}$	6234 ± 472$^{\#}$	6208 ± 465$^{\#}$
HF							
BW, g	25.7 ± 1.1	26.2 ± 1.1	25.3 ± 1.1	25.6 ± 1.2	25.5 ± 0.9	26.1 ± 1.2	26.7 ± 1.3
HR, bpm	488 ± 46	478 ± 35	484 ± 46	475 ± 38	482 ± 48	488 ± 58	462 ± 44
HW/BW, mg/g	**8.1 ± 0.6**	**7.8 ± 0.5$^{\#}$**	**9.2 ± 0.6**	**7.6 ± 0.4$^{\#}$**	**8.4 ± 0.5**	**8.2 ± 0.7$^{\#}$**	**7.9 ± 0.6$^{\#}$**
LW/BW, mg/g	**7.3 ± 0.4$^{\#}$**	**6.5 ± 0.4*,$^{\#}$**	**8.6 ± 0.5***	**6.4 ± 0.4*,$^{\#}$**	**7.6 ± 0.5**	**7.2 ± 0.6$^{\#}$**	**6.7 ± 0.5$^{\#}$**
EF, %	**37.15 ± 0.3$^{\#}$**	**45.15 ± 0.6*,$^{\#}$**	**31.06 ± 0.4***	**42.11 ± 0.4*,$^{\#}$**	**35.02 ± 0.3*,$^{\#}$**	**36.91 ± 0.5$^{\#}$**	**40.51 ± 0.7$^{\#}$**
FS, %	**18.64 ± 0.3$^{\#}$**	**21.76 ± 0.4*,$^{\#}$**	**15.12 ± 0.3***	**20.14 ± 0.4$^{\#}$**	**17.64 ± 0.3*,$^{\#}$**	**17.81 ± 0.4$^{\#}$**	**19.96 ± 0.6$^{\#}$**
DBP, mmHg	81.62 ± 2.6	83.4 ± 2.9	80.61 ± 2.5	81.45 ± 2.3	81.5 ± 2.1	80.96 ± 3.1	82.48 ± 2.8
dP/dt$_{max}$, mmHg/s	**5881 ± 402$^{\#}$**	**6752 ± 466*,$^{\#}$**	**3946 ± 384***	**6728 ± 442*,$^{\#}$**	**5520 ± 433$^{\#}$**	**5872 ± 464$^{\#}$**	**6432 ± 482$^{\#}$**
dP/dt$_{min}$, mmHg/s	**5006 ± 398$^{\#}$**	**5834 ± 422*,$^{\#}$**	**3348 ± 362***	**5866 ± 408*,$^{\#}$**	**4718 ± 416$^{\#}$**	**5086 ± 412$^{\#}$**	**5766 ± 474$^{\#}$**
Serum TnI, ng/mL	62.4 ± 12.5	61.8 ± 10.2	61.5 ± 11.8	61.2 ± 10.5	62.4 ± 12.5	60.6 ± 10.8	61.1 ± 12.8
Infarct size, % of LV	43.6 ± 4.4	42.2 ± 4.3	39.7 ± 3.9	42.8 ± 4.6	41.1 ± 4.3	43.1 ± 4.5	43.8 ± 4.1

BW, body weight; DBP, diastolic blood pressure; d*P*/dt$_{max}$, maximum derivative of change in pressure rise over time; d*P*/dt$_{min}$, maximum derivative of change in pressure fall over time; EF, ejection fraction; FS, fractional shortening; HR, heart rate; HW, heart weight; LW, lung weight; TnI, Troponin I measured 1 d after coronary artery ligation; *n* = 16–20 mice per group for echo, BW, HW/BW, LW/BW, and TnI measurements, *n* = 6–7 mice per group for hemodynamic measurements; measurements reported in the second section of the table (HF) were obtained 4 wk after myocardial infarction (MI); infarct size is expressed as % of left ventricle (LV) in distinct groups of mice (5–6 mice per group, 5-mo-old), 2 d post-MI. Parameters that are significantly different (*P* < 0.05, two-tailed *t* test) compared with SHAM conditions are reported in bold. **P* < 0.05 vs. WT, $^{\#}$*P* < 0.05 vs. RyR2-2808D, ANOVA, Tukey–Kramer post hoc test.

Table S2. Primer sequences

Gene	Forward 5′–3′	Reverse 5′–3′	Product size, bp
IP3R1	TGGTCCAGCACTTTGTTCAC	TCTGCCTTGACAATCGTCTG	85
IP3R2	AGACTCTCAGCTCGCTCTGG	GGCCACGACATCCTGTAACT	99
IP3R3	ACATCCTGGCTGAAGACACC	AAAGGTCTCCACCTCCGTCT	92
Actin	CTCTTCCAGCCTTCCTTCCT	AGCACTGTGTTGGCGTACAG	116
H19	GTACCCACCTGTCGTCC	GTCCACGAGACCAATGACTG	207
18S	CGCGGTTCTATTTTGTTGGT	AGTCGGCATCGTTTATGGTC	219
mt12S	ACCGCGGTCATACGATTAAC	CCCAGTTTGGGTCTTAGCTG	178
mt16S	CCTTGTTCCCAGAGGTTCAA	ATGCCGTATGGACCAACAAT	169